

# Modeling and Design of Microjet Actuators

Duncan A. Lockerby\*

*King's College London, London, England WC2R 2LS, United Kingdom*  
and

Peter W. Carpenter†

*University of Warwick, Coventry, England CV4 7AL, United Kingdom*

**A computational model is developed to aid the design of microelectromechanical systems (MEMS) for use in active turbulence control. The focus here is on micro-actuators and, in particular, a design employed by synthetic-jet devices. This consists of a diaphragm within a cavity that, by its piezoinduced motion, creates an ejection of fluid through an orifice in the cavity's lid. The diaphragm is modeled using classical thin-plate theory, with the stiffness of the attached piezodevice incorporated. For numerical economy, the fluid motion within the cavity is not modeled; instead, the pressure is calculated with the perfect gas law. However, in the orifice, where viscous forces are more dominant, one-dimensional Navier–Stokes equations are solved. The actuator system is modeled in its entirety. All that is required to calculate the outlet jet velocity is the input voltage applied to the piezodevice. The numerical model is validated against experimental data for synthetic-jet devices and used to predict their optimal dimensions. An alternative mode of forcing the diaphragm is proposed that does not suffer from the drawbacks inherent in synthetic-jet operation at MEMS scale. This mode generates a jump in cavity pressure, creating a pufflike jet disturbance. This concept is explored with the aim of uncovering practical issues and simple design guidelines.**

## Introduction

COHERENT structures in the near-wall region of a turbulent boundary layer, notably observed by Kline et al.,<sup>1</sup> are generally thought to be critical to the generation of turbulence.<sup>2</sup> If this is the case, then amplifying or canceling these structures (or streaks, as they are commonly known) should have a similar effect on the overall level of turbulence. In principle, then, a simple method for the control of turbulence exists, by targeting streaks.

There would be substantial reward if targeted control of turbulence could be realized over an airfoil, for example, the reduction of skin friction or the delay of boundary-layer separation. However, owing to the small scales demanded by the application, it is only since the advent of microelectromechanical systems (MEMS) that targeted control has been considered seriously.

MEMS are devices with electrical and mechanical components, fabricated to micrometer scale by the use of integrated-circuit batch-processing techniques. This relatively new technology has already produced many MEMS devices of practical significance. Examples include the fabrication of microgrippers for medical applications, miniature sensors for airbag control, and micrometer-sized neuron probes.

Application of MEMS technology to the turbulence control application is at a preliminary stage of development. Little is known about how the miniaturized flow-control devices will perform. The present paper explores the behavior of a popular MEMS–actuator concept and addresses the hitherto unconsidered issues of designing MEMS actuators for turbulence control.

## Demands of Targeted Control

The turbulence-control application dictates a very challenging sensor and actuator specification. Here, only the demands on the

actuator's dimensions and response rate are considered. (For sensor requirements see Ref. 3.)

Before actuator dimensions can be proposed, typical flight conditions must be defined. For an aircraft at cruise speed (at sea level) the following values can be estimated:  $U_\infty$  (freestream velocity) =  $300 \text{ m} \cdot \text{s}^{-1}$ ,  $v^*$  (friction velocity) =  $10 \text{ m} \cdot \text{s}^{-1}$ ,  $\nu$  (kinematic viscosity) =  $15 \text{ mm}^2 \cdot \text{s}^{-1}$ , and  $\nu/v^*$  (the wall unit) =  $1.5 \mu\text{m}$ . For the rest of this paper, these values will be referred to as flight-scale conditions. Strictly speaking, the kinematic viscosity corresponding to a typical cruise altitude should have been used, but this would not have altered the estimates greatly.

The average spanwise spacing of the low-speed streaks is widely quoted as being  $100\nu/v^*$  (Ref. 1) and the length of streaks up to 10 times this.<sup>2</sup> In flight conditions, this equates to a  $150\text{-}\mu\text{m}$  streak spacing and a  $1.5\text{-mm}$  streak length. If an actuator is to manipulate streaks individually, it would need to be a fraction of their average spanwise spacing. Hence, for a circular jet, a suitable orifice diameter would be no greater than  $40\nu/v^*$  ( $60 \mu\text{m}$ ). Devices of such scale were not a possibility until the fabrication technologies of MEMS, and, even so, no such device has yet been employed as a flow-control actuator.

Temporal demands are also placed on the actuators by the bursting frequency of the streaks. If it is assumed that the frequency scales with inner variables (though this has been contended<sup>4</sup>) the average time between bursts, at flight scale, would be approximately  $25 \mu\text{s}$  ( $f = 260 \text{ kHz}$  and  $f^+ = 0.04$ ; Ref. 5). If an actuator is to be successful in controlling single coherent structures, its duration should be a fraction of this period because the streaks convect quickly downstream and can drift in the spanwise direction. (Johansson et al.<sup>6</sup> calculated an average convection speed of  $10v^*$ .)

In an array of actuators, separated by  $150 \mu\text{m}$  in the spanwise direction (the average streak spacing) and  $1.5 \text{ mm}$  in the streamwise direction (the average streak length), the number of devices required to cover a  $1\text{-m}^2$  surface area would be in excess of four million. If each actuator performed control every 10 burst periods, then, in total (for the  $1\text{-m}^2$  array), there would be almost 20 billion actuation instances per second. This simple analysis demonstrates the inherent difficulty involved with MEMS-based turbulence control. Nevertheless, intelligent control of whatever kind should reduce the density of the array and the frequency of actuation required to produce a positive effect on aerodynamic performance.

Received 24 July 2002; revision received 27 August 2003; accepted for publication 26 August 2003. Copyright © 2003 by the American Institute of Aeronautics and Astronautics, Inc. All rights reserved. Copies of this paper may be made for personal or internal use, on condition that the copier pay the \$10.00 per-copy fee to the Copyright Clearance Center, Inc., 222 Rosewood Drive, Danvers, MA 01923; include the code 0001-1452/04 \$10.00 in correspondence with the CCC.

\*Research Associate, Department of Mechanical Engineering, Strand.

†Professor of Mechanical Engineering, Fluid Dynamics Research Center. Senior Member AIAA.

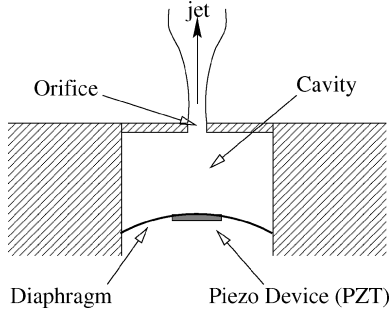


**Fig. 1** Schematic of a synthetic-jet actuator diaphragm-cavity design.

### Synthetic-Jet Technology

It is known that oscillating velocity fields can generate jets via a mechanism akin to acoustic streaming (reviewed by Lighthill<sup>7</sup>). Jets generated by such streaming mechanisms are referred to as synthetic jets, also known as massless or zero-mass jets.

The popularity of synthetic-jet actuators stems from their self-contained design; no fluid source or ducting is required, only an applied voltage. For this reason, and owing to their success with separation delay,<sup>8–10</sup> synthetic jets are now being considered for the turbulence-control application. Figure 1 shows a generic synthetic-jet design, here referred to as the diaphragm-cavity actuator. The device consists of a diaphragm, set within a cavity, that is driven by a piezoelectric (or electrostatic) force at its resonant frequency. An orifice in the lid of the device allows fluid to be drawn into, and forced out of, the cavity.

Despite synthetic jets' success in large-scale streak control,<sup>11,12</sup> there are two major problems with using the concept at flight scale. The first is the very high driving frequency needed to establish a synthetic jet in time to control streaks individually, at least an order of magnitude greater than the bursting frequency. The second major problem with MEMS-scale synthetic-jet actuators is the risk of dust clogging the device during the inflow cycle. Aircraft manufacturers see this as a serious issue because cleaning MEMS would be an incredibly demanding operation.

Not all MEMS designs need suffer from these drawbacks. For example, the microvalves of Vandelli et al.<sup>13</sup> and Yang and Kao<sup>14</sup> close automatically after operation. Microvalves, however, require a fluid source and a ducting network.

In this paper, an alternative mode of forcing the diaphragm-cavity device is suggested. This forcing mode allows the self-contained actuator design to be used, but does not suffer from the drawbacks of synthetic-jet operation. Mathematical and numerical models have been developed for the purpose of exploring this design concept.

### Actuator Modeling

For the purposes of modeling, the diaphragm-cavity design of Fig. 1 can be viewed as four distinct subsystems; a diaphragm, a piezoelectric disk, a cavity, and an orifice. The mathematical modeling and the numerical implementation of each is considered in this section.

#### Diaphragm

The diaphragm has been modeled with classical thin-plate theory. This provides an accurate description of the diaphragm dynamics and allows arbitrary diaphragm-forcing modes to be modeled.

For a thin elastic plate, with an applied-pressure function  $P$ , the equation of motion for axisymmetric deflection is given by

$$\rho_d t_d \ddot{w} + d\dot{w} + B\nabla^2 \nabla^2 w = P - P_c \quad (1)$$

where  $w$  is the deflection (dot notation denotes a temporal derivative),  $\rho_d$  is the diaphragm density,  $t_d$  is the diaphragm thickness,  $B$  is the flexural rigidity,  $d$  is the structural damping, and  $P_c$  is the pressure in the cavity. For axisymmetric disturbances, the biharmonic

operator  $\nabla^2 \nabla^2$  and the flexural rigidity  $B$  are defined as follows:

$$B = \frac{Et_d^3}{12(1-\nu^2)} \quad (2)$$

$$[\nabla^2 \nabla^2] \equiv \left[ \frac{\partial^4}{\partial r^4} + \frac{2}{r} \frac{\partial^3}{\partial r^3} - \frac{1}{r^2} \frac{\partial^2}{\partial r^2} + \frac{1}{r^3} \frac{\partial}{\partial r} \right] \quad (3)$$

where  $r$  is the radial coordinate,  $E$  is the elastic modulus, and  $\nu$  is Poisson's ratio.

For numerical solution, Eq. (1) is discretized with second-order centered differences and a Crank–Nicholson time-stepping scheme. The resulting set of equations are solved implicitly with lower–upper decomposition.

The boundary conditions at the edge of the diaphragm are simply zero deflection and zero gradient. (The plate is clamped at its edge.) At the centerpoint of the diaphragm, a condition of symmetry is enforced.

For the simulations presented in this paper, the time step used is around two orders of magnitude smaller than the time taken for the diaphragm to reach its maximum deflection. Spatially, around 20 grid points over the diaphragm's radius have been used. This is sufficient resolution because structural damping tends to eliminate vibration at frequencies above the fundamental mode.

#### Piezoelectric Disk

The stiffness of the piezoelectric device (PZT) directly affects the dynamic characteristics of the plate structure as a whole. To accommodate this within the classical model [Eq. (1)], an effective flexural rigidity  $B_e$  is calculated that combines the stiffness of both the PZT and diaphragm. If it is assumed that the strain varies linearly through the cross section, and the net lateral force (perpendicular to the motion of the diaphragm) is zero, the following expression can be obtained:

$$B_e = \frac{[E_d(t_d - z_n)^3 + E_p(t_p + z_n)^3 + z_n^3(E_d - E_p)]}{3(1 - \nu_e^2)} \quad (4)$$

where  $E_d$ ,  $t_d$ ,  $E_p$ , and  $t_p$  are the elastic moduli and material thickness of the diaphragm and PZT, respectively. The position of the neutral surface  $z_n$  is given by

$$z_n = \frac{1}{2} \left( \frac{E_d t_d^2 - E_p t_p^2}{E_d t_d + E_p t_p} \right) \quad (5)$$

The effective Poisson's ratio  $\nu_e$  can be calculated by ensuring that the energy in the composite section is equal to the internal energy that would be produced by the two materials independently.

Incorporating the effective rigidity  $B_e$  into the discretized form of Eq. (1) requires the inclusion of midplate boundary conditions. These are needed to enforce the continuity of bending moment, vertical shear, and deflection gradient.

The electrostrictive force generates a lateral response. This makes it difficult to model using the classical plate equation (1), which only describes vertical deflection. However, the vertical response can be estimated if it is assumed that the lateral deflection is instantaneous and creates an internal moment that is independent of bending. This moment can be numerically implemented by a fictitious vertical forcing. (See Ref. 15 for details.)

#### Orifice

An increasing amount of effort is being dedicated to the research of microfluidic effects in the field of MEMS.<sup>16,17</sup> The main concern for modeling purposes is whether the continuum approximation is valid, and, if not, how does the rarefied flow behave? Such considerations are important when the mean free path of the gas,  $\lambda$ , the average distance between molecular collisions, is comparable to the characteristic length of the flow,  $L$ . The degree of gas rarefaction is expressed by the Knudsen number  $Kn$ :

$$Kn = \lambda/L \quad (6)$$

The continuum assumption and the Navier–Stokes equations are valid only when  $Kn < 0.01$ . Beyond this, the slip flow regime is encountered ( $0.01 < Kn < 0.1$ ), where the no-slip condition at wall interfaces is no longer satisfied. The transition regime is when  $0.1 < Kn < 3$ , and then completely rarefied or free-molecular flow occurs for  $Kn > 3$  (Ref. 18).

For the present application, the characteristic length is taken to be the orifice diameter and the mean free path of air as  $\lambda = 0.065 \mu\text{m}$ . To control streaks individually, at flight scale, the orifice diameter would need to be of the order of  $10 \mu\text{m}$ . This gives a Knudsen number of  $Kn = 0.0065$ , thus satisfying the continuum criterion and allowing the Navier–Stokes equations to be used. For orifice diameters that border the slip-flow regime, slip boundary conditions, such as those due to Maxwell and Smoluchowski, could be used to obtain improved results (see Ref. 17). However, these have not been considered in the present study because our main interest lies in larger devices.

For axisymmetric parallel flow in a circular orifice, the Navier–Stokes equations are

$$\frac{\partial \rho}{\partial t} + \frac{\partial(\rho u)}{\partial x} = 0 \quad (7)$$

$$\frac{\partial(\rho u)}{\partial t} + \frac{\partial(\rho u^2)}{\partial x} = -\frac{\partial p}{\partial x} + \mu \nabla^2 u \quad (8)$$

where  $x$  is the axial coordinate,  $t$  is time,  $u$  is the axial velocity,  $\rho$  is the density,  $p$  is the pressure, and  $\nabla^2$  is the Laplacian operator given by

$$\nabla^2 \equiv \left[ \frac{1}{r} \frac{\partial}{\partial r} + \frac{\partial^2}{\partial r^2} \right] \quad (9)$$

where  $r$  is the radial coordinate.

For simplicity, fully developed pipe flow in the orifice has been assumed. (Ideally the full three-dimensional compressible equation set should be solved.) This neglects the developing region of the pipe flow and implies the instantaneous application of a constant (down-the-pipe) pressure gradient and, therefore, a linear variation of pressure. This is only an accurate assumption when the length of the pipe is large in comparison to its radius. Also, because of the comparatively low flow speeds, it is fair to assume that variations in the density and velocity through the pipe are small. Consequently, linear variations of density and velocity are fair, though not exact, approximations.

The linear approximations to density, pressure, and velocity allow a calculation of one-dimensional order, where Eq. (7) and (8) are expressed in the following form:

$$u_2 = \frac{\rho_1 u_1}{\rho_2} - \frac{l}{2\rho_2} \frac{\partial \rho_1}{\partial t} \quad (10)$$

$$\frac{\partial u_1}{\partial t} + \left( \frac{\rho_1}{\rho_2} - 1 \right) \frac{u_1^2}{l} - \frac{u_1}{2\rho_2} \frac{\partial \rho_1}{\partial t} = \frac{p_1 - p_2}{l\rho_1} + \frac{\mu}{\rho_1} \nabla^2 u_1 \quad (11)$$

where  $l$  is the orifice length and the subscripts one and two denote values at the inlet and outlet, respectively. Note that the fluid at the outlet is assumed to be incompressible. All density variation occurs within the cavity and orifice. The second and third terms on the left-hand side of Eq. (11) are nonlinear and result from the compressibility of fluid in the orifice. Their influence, however, is only slight.

Equation (11) is discretized with second-order centered differences and expressed in  $\Delta$  form.<sup>19</sup> This produces a tridiagonal set of equations, enabling the use of the numerically efficient Thomas algorithm. For the majority of simulations, 20 grid points were sufficient to capture the flow details to an acceptable degree of accuracy.

### Cavity

The cavity is the lever between the plate motion and jet expulsion. Its behavior is central to the system. Ideally, if computational

efficiency were not an issue, the full compressible Navier–Stokes equations would be solved in both the cavity and the orifice.<sup>20</sup> Here, an economical alternative, originally employed by Rathnasingham and Breuer,<sup>21</sup> has been adopted. This model assumes that inside the cavity the fluid-dynamic effects are negligible and that the compression is isothermal and instantaneous. Although this is numerically economical, it is not appropriate in all cases. For example, when the cap area of the cavity is of comparable order to the orifice area, and incompressible flow is assumed, the flow rates in the orifice and cavity will also be comparable. If, therefore, the cavity fluid dynamics is to be safely neglected, the orifice area must be significantly smaller than the area of the cavity cap.

With this model, the rate of change of cavity density is given by

$$\frac{d\rho_c}{dt} = \frac{\rho_c}{V} \frac{dV}{dt} + \frac{1}{V} \frac{dM}{dt} \quad (12)$$

where  $\rho_c$  is the cavity density,  $V$  is the cavity volume, and  $M$  is the mass of fluid in the cavity.

Equation (12) is solved for the cavity density  $\rho_c$  with a predictor–corrector scheme, where the values of  $V$ ,  $dV/dt$ , and  $dM/dt$  are obtained from the implicit diaphragm and orifice solutions. The size of the time step is governed by the diaphragm model because temporal variations in the diaphragm tend to be equal or on a shorter scale to variations in cavity pressure.

### Model Validation

Rizzetta et al.<sup>20</sup> have shown that vortices are generated within the cavity during the inflow cycle of a synthetic jet; mainly for this reason, the current model, which was not originally designed for synthetic-jet simulations, could not necessarily be expected to provide accurate predictions for the synthetic jet. Despite this deficiency, the present model appears to give results that compare well with the empirically determined characteristics of the synthetic jets of Crook et al.<sup>10</sup> Owing to the general lack of data for diaphragm–cavity actuators, the data of Crook et al.<sup>10</sup> have been used for the purposes of model validation. Accordingly, it would appear that the present model, despite its deficiencies, can be used as an effective design tool for synthetic jets.

The actuator of Crook et al.<sup>10</sup> was a diaphragm–cavity synthetic jet similar to the one shown in Fig. 1, except that the exit orifice was located on the side rather than the lid opposite the diaphragm. Material properties and dimensions of the device are as follows: cavity height  $H = 2 \text{ mm}$ , orifice length  $l = 1.6 \text{ mm}$ , diaphragm radius  $R_d = 12.7 \text{ mm}$ , PZT radius  $R_p = 11 \text{ mm}$ , diaphragm thickness  $t_d = 0.1 \text{ mm}$ , PZT thickness  $t_p = 0.1 \text{ mm}$ , diaphragm elastic modulus  $E_d = 110 \text{ GPa}$ , PZT elastic modulus  $E_p = 63 \text{ GPa}$ , diaphragm Poisson's ratio  $\nu_d = 0.35$ , PZT Poisson's ratio  $\nu_p = 0.3$ , diaphragm density  $\rho_d = 8520 \text{ kg} \cdot \text{m}^{-3}$ , PZT density  $\rho_p = 7600 \text{ kg} \cdot \text{m}^{-3}$ , and structural damping factor  $d = 7 \text{ kN} \cdot \text{s} \cdot \text{m}^{-3}$ .

The diaphragm and PZT disks used in the experiments were factory made and, presumably, optimized to some extent for performance. The optimum PZT size (defined as the PZT thickness and radius, which, for a given diaphragm size, produces the greatest overall deflection) can be predicted using the numerical model. The optimum PZT thickness was found to be  $t_p = 126 \pm .5 \mu\text{m}$  (26% deviance from the actual PZT thickness) and the optimum PZT radius found to be  $R_p = 10.9 \pm 0.5 \text{ mm}$  (within 1% of the actual PZT radius). Details of these simulations are given in Ref. 15, where it is also shown that the optimum ratio of PZT and diaphragm radius is independent of scale and proportion.

Numerical simulations were performed to calculate the resonant frequency of the combined PZT and diaphragm. Figure 2 shows the comparison of the numerical solution and the value observed experimentally (1366 Hz); very close agreement is found.

At large orifice radii, a simple incompressible treatment of the cavity provides a more accurate model than the compressible numerical solution. Here a combined model is used that, at some critical radius, abruptly switches between the compressible and the incompressible model. (In reality one would expect a smooth transition between the behaviors captured by the two different schemes.) This

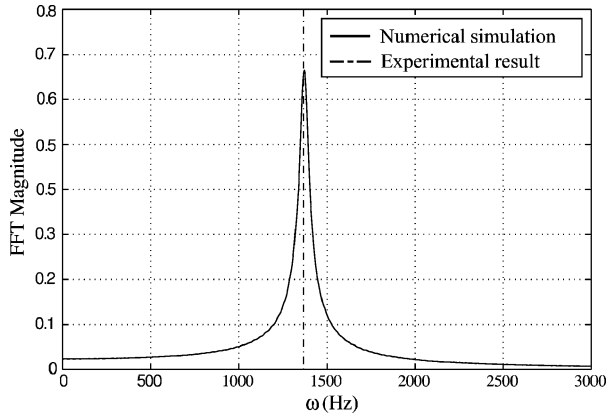


Fig. 2 Resonant frequency of the PZT and diaphragm: ---, experimental data and —, numerical simulation, simulation parameters: time step  $\Delta t = 2.5 \mu s$  and number of diaphragm grid points  $N_d = 80$ .

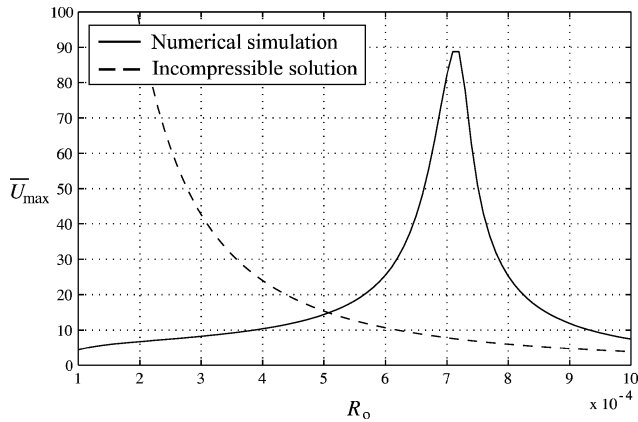


Fig. 3 Maximum average velocity (maximum over time, average over orifice cross section  $\bar{U}_{\max}$ ) against orifice radius  $R_o$  —, numerical solution and --- incompressible solution.

critical radius is chosen such that the velocities predicted by the compressible and incompressible solution are equal in magnitude, indicating that the two behaviors have roughly comparable influence. At this point in the combined model, there occurs a peak in the velocity magnitude and, therefore, an optimum (defined here as the orifice size that produces the greatest instantaneous velocity outflow averaged over the orifice cross section). This method of optimization is similar to that employed by Rathnasingham and Breuer<sup>21</sup> who equated an incompressible solution with a compressible solution to successfully predict an optimum Stokes parameter for their actuator.

Note that the magnitude of velocity calculated at this point will be a significant overestimate because each model is at the limit of its applicability. Figure 3 shows the variation of maximum velocity with orifice radius calculated by both the numerical model and the simple incompressible solution. The intersection (where the two models predict equal velocity magnitudes) occurs at an orifice radius of approximately 0.51 mm, which is in excellent agreement with the empirically determined optimum; Crook et al.<sup>10</sup> found an optimum orifice radius  $R_o$  of  $0.5 \pm 0.05$  mm.

The same method can be employed to calculate the optimum cavity height (that which produces the greatest average velocity output). In this instance, the orifice radius is fixed at  $R_o = 0.6$  mm. Figure 4 shows the variation of maximum velocity predicted by the numerical model and the incompressible solution. The intersection occurs at a cavity height of 2.8 mm, which compares very closely with the experimental optimum of  $H = 3 \pm 0.5$  mm.

The results in this section are encouraging for two reasons: first, because it is clear that the numerical code and mathematical model are sound and accurate and, second, because, though it was not

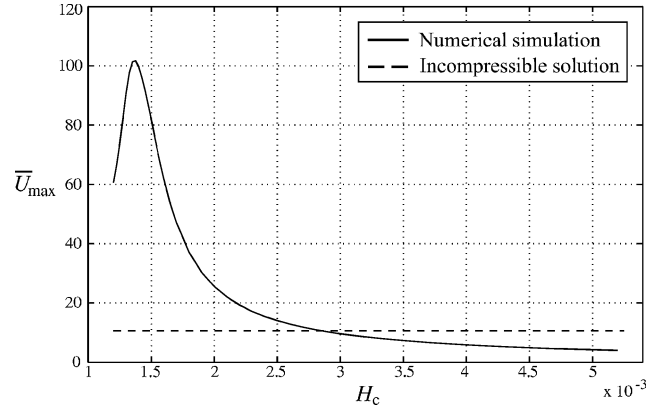


Fig. 4 Maximum average velocity (maximum over time, average over orifice cross section  $\bar{U}_{\max}$ ) against cavity height  $H$ : —, numerical solution and ---, incompressible solution.

developed for this purpose, the model can be used as an effective design tool for synthetic-jet actuators.

### Pressure-Jump Actuators

A rapidly deflecting diaphragm can produce a sudden jump in the cavity pressure. Such a pressure jump will, in some cases, produce a single puff of fluid out through the orifice. This response does not have the drawbacks of synthetic-jet actuation and is investigated here. Furthermore, provided that the conditions for Helmholtz resonance (given later) are not satisfied, there is strong outflow and only very weak inflow. Under these circumstances, neglecting the fluid flow within the cavity is likely to be a much better approximation than it was for a synthetic jet.

To generate a rapid deflection, a step force (or voltage) is applied to the diaphragm, which, after actuation, can be slowly relaxed to its nondeflected state. In an undamped diaphragm, this causes strong vibration at many frequencies; for an optimal response, a critical level of diaphragm damping is required. Alternatively, microvalves could be employed to provide the initial pressure jump, but because a fluid source would be needed, the device's self-containment would then be lost.

To demonstrate the typical behavior of a pressure-jump device, some dimensions have been chosen (here expressed in terms of a characteristic length scale  $g$ ): height of the cavity  $H = 50g$ , radius of the diaphragm  $R_d = 50g$ , thickness of the diaphragm  $t_d = 1g$ , PZT radius  $R_p = 43g$ , PZT thickness  $t_p = 1.22g$ , and orifice length  $l = 10g$ .

Figure 5 shows velocity outputs from pressure-jump actuators (for  $g = 1 \mu m$ ) of varying orifice radii. The strong viscous forces developed in a small orifice (Fig. 5a;  $R_o = 3.8 \mu m$ ) reduce the maximum velocity and lengthen the period of actuation. A larger orifice (Fig. 5d;  $R_o = 9.8 \mu m$ ) produces a greater velocity, but also exhibits an oscillation. This oscillation, which is not a consequence of diaphragm motion, has an impact on the design of all cavity-driven actuators.

### Helmholtz Condition

It can be shown by standard analysis<sup>22</sup> that the frequency of unforced pressure fluctuation in a cavity with an orifice is given by

$$\omega = \sqrt{\frac{\pi R_o^2 k T}{l V}} \quad (13)$$

where  $k$  is the gas constant,  $T$  is the temperature,  $l$  is the orifice length,  $V$  is the cavity volume, and  $R_o$  is the orifice radius. This is the Helmholtz frequency, and for an inviscid orifice flow, it is the preferred frequency of pressure variation in the cavity. Pressure fluctuations of this kind are the source of the velocity oscillation shown in Fig. 5d. This phenomenon will be referred to here as Helmholtz oscillation.

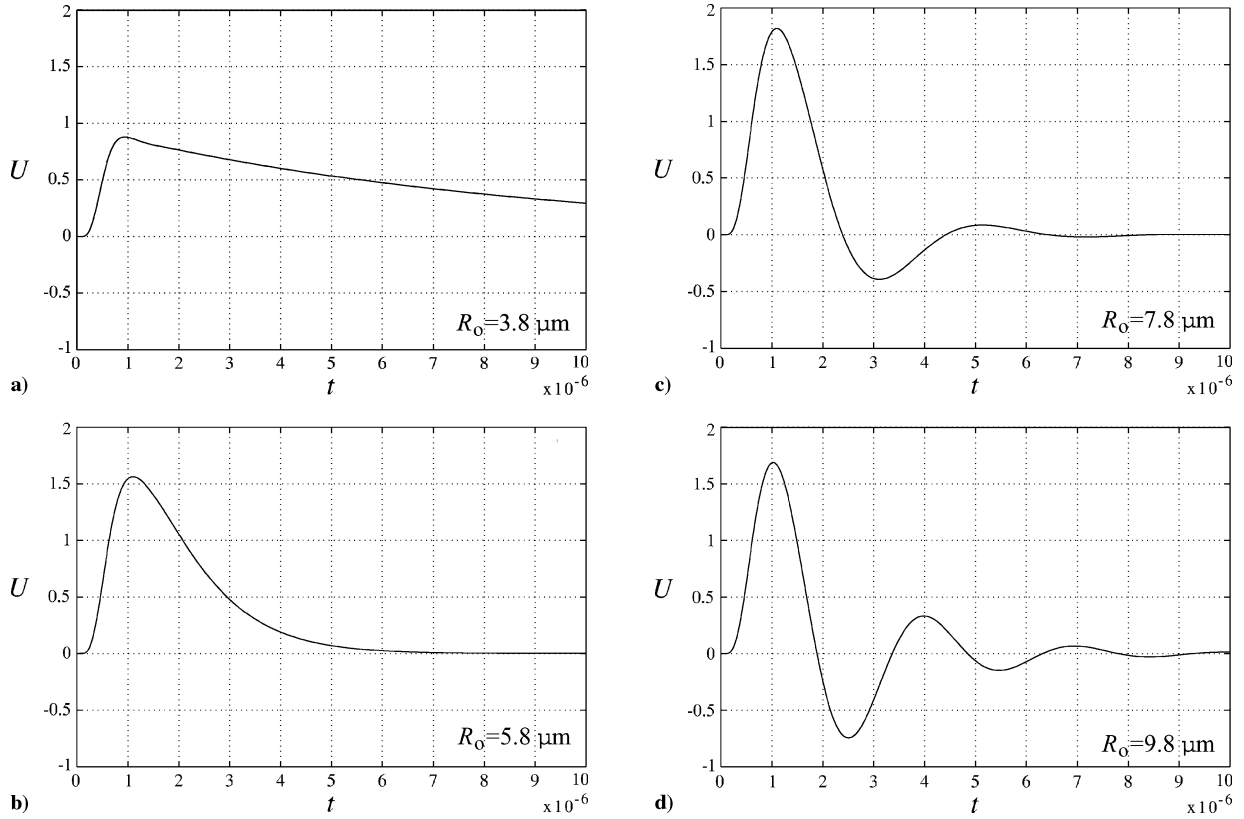


Fig. 5 Velocity output  $U$  from pressure-jump actuators with varying orifice radii: a)  $R_o = 3.8 \mu\text{m}$ , b)  $R_o = 5.8 \mu\text{m}$ , c)  $R_o = 7.8 \mu\text{m}$ , and d)  $R_o = 9.8 \mu\text{m}$ .

The point at which viscosity is just sufficient to dampen this oscillation (the viscous threshold) is important to quantify for two reasons. First, if strong oscillation occurs, there will be significant flux into the cavity. This is undesirable because of the risk of inhaled dust clogging the system. The second concern is that the device would have the potential for Helmholtz resonance. This occurs when imposed pressure variations, perhaps from the boundary layer, coincide with the Helmholtz frequency and cause large mass flow rates in and out of the cavity. In a boundary layer, this could cause unpredictable effects, such as the early onset of laminar-to-turbulent transition; in general, it is undesirable for an active control device to be triggered by external influences.

At the viscous threshold, the flow will be fully developed but will also have the potential for unsteadiness. This flow regime can be described by unsteady Poiseuille flow:

$$\frac{dU}{dt} = \frac{3\Pi}{2\rho_a} - \frac{6\nu U}{R_o^2} \quad (14)$$

where  $U$  is the centerline velocity,  $\Pi$  is the unsteady pressure gradient,  $\rho_a$  is the ambient density, and  $\nu$  is the kinematic viscosity. [This can be derived from Eq. (11) if compressible effects are neglected and a parabolic velocity profile is assumed]. Equation (14) can be expressed in terms of the mass flow rate through the orifice  $Q$  and the pressure inside and outside of the cavity,  $P_c$  and  $P_a$ :

$$\frac{dQ}{dt} = \frac{3\pi R_o^2}{4l}(P_c - P_a) - \frac{6\nu Q}{R_o^2} \quad (15)$$

The relationship between cavity pressure and the mass flow rate is given by

$$\frac{dP_c}{dt} = -\frac{QkT}{V} \quad (16)$$

which can be substituted into Eq. (15) to obtain a second-order differential equation describing the temporal variation in cavity

pressure:

$$\frac{d^2 P_c}{dt^2} = -\frac{3\pi R_o^2 kT}{4lV}(P_c - P_a) - \frac{6\nu}{R_o^2} \frac{dP_c}{dt} \quad (17)$$

This has a solution in the form

$$P_c = P_a + Ae^{i\omega t} \quad (18)$$

which, when substituted into Eq. (16), yields the following auxiliary equation:

$$\omega^2 - \frac{6\nu}{R_o^2}i\omega - \frac{3\pi R_o^2 kT}{4lV} = 0 \quad (19)$$

Helmholtz oscillation can only occur when the roots of Eq. (19) have a real component. This will be referred to as the Helmholtz condition:

$$R_o > \left( \frac{12\nu^2 lV}{\pi kT} \right)^{\frac{1}{6}} \quad (20)$$

If the Helmholtz condition is satisfied, then the Helmholtz frequency  $\alpha$  and the decay rate  $\lambda$  are as follows:

$$\alpha = \sqrt{\frac{3\pi R_o^2 kT}{4lV} - \frac{9\nu^2}{R_o^4}}, \quad \lambda = \frac{3\nu}{R_o^2} \quad (21)$$

A series of numerical simulations have been performed to validate the Helmholtz condition predicted by Eq. (20). This is done by varying the orifice radius until, at some point during the actuation period, a negative velocity is observed; at this point it can be assumed that Helmholtz oscillation is occurring.

Figure 6 shows the variation of minimum average velocity (minimum over time; average over the cross section) with orifice radius, for a particular cavity-driven actuator ( $g = 625 \mu\text{m}$ ). The numerical results ( $\square$ ) show that a negative velocity and, therefore, oscillation occur when  $R_o > 430 \mu\text{m}$ ; the analytically obtained Helmholtz condition ( $\cdots$ ) is in exact agreement with this.

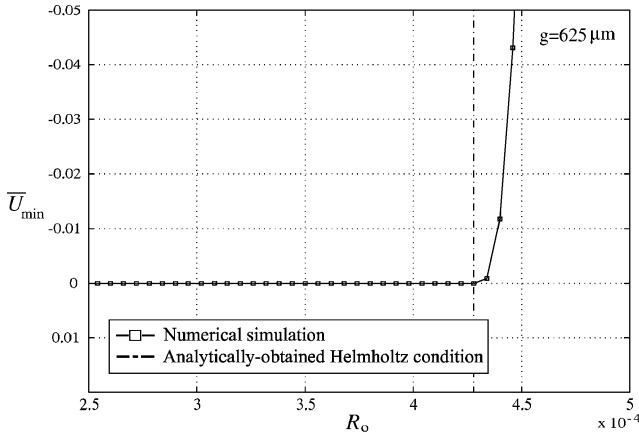


**Fig. 6** Minimum average velocity (minimum over time, average over orifice cross section  $\bar{U}_{\min}$ ), obtained from a pressure-jump actuator ( $g = 625 \mu\text{m}$ ),  $\square$ , with varying orifice radius  $R_o$  and  $---$ , the analytically obtained Helmholtz condition.

### Actuator Design

It has been demonstrated by Lockerby et al.<sup>23</sup> that for pressure-jump actuators, and many similar devices, the most important jet characteristic is the total mass outflow (the net flux). This is maximized by making the volume displacement of the diaphragm or pressure valve as large as possible. This section details how the remaining design parameters, such as orifice radius, can be set to achieve maximum jet velocity for a given net flux. The optimization in this section is relevant to both diaphragm-driven and microvalve-driven pressure-jump actuators, as well as devices in synthetic-jet operation.

Note that the form of the flow structure generated by such devices may have a significant influence on their overall effectiveness. However, from a design perspective, this is not something that can be controlled directly because the flow structures will be heavily influenced by the external flowfield.

### Optimization

As an aid for preliminary design calculations, a heuristic analytical method is proposed. This will be validated later by making comparisons with numerical simulations.

There are essentially two extreme actuator flow regimes; for small orifices, the flow is dominated by viscous effects, and for large orifices, inviscid Helmholtz resonance dominates. Actual flows usually exhibit a combination of both flow behaviors. The simplification that is made for the heuristic analytical method is to assume that small orifices exhibit purely viscous behavior and that, as the orifice size is increased, at a certain threshold value the flow behavior suddenly jumps to purely inviscid behavior. It seems reasonable to assume that this jump will occur when the inviscid and viscous flow regimes produce the same predicted orifice velocity, indicating that the two effects are roughly equal in influence. In Fig. 3, this condition occurs at about  $R_o = 0.5 \text{ mm}$ . Essentially, it is assumed that for smaller orifice sizes the high outflow speeds predicted by the inviscid theory will be suppressed by viscous effects and that, for larger orifice sizes, the high outflow regime predicted by purely viscous theory will be replaced by a flow dominated by Helmholtz resonance. The heuristic method relies on setting the two approximate analytical predictions for outflow velocity equal to obtain a simple analytical expression for the optimal orifice radius.

For optimum performance, synthetic jets should be designed so that the diaphragm frequency is equal to the resonant, that is, Helmholtz, frequency of the cavity. In the case of pressure-jump actuators, the flow also oscillates at the Helmholtz frequency in the purely inviscid regime, so that the unsteady flow equation in both cases is

$$\frac{d\bar{U}}{dt} = \frac{\Pi}{\rho_a} \quad (22)$$

where  $\bar{U}$  is the average velocity that is, averaged over the orifice cross section and  $\Pi$  is the pressure gradient:

$$\Pi = (\Delta P/l)e^{i\omega t} \quad (23)$$

where  $\Delta P$  is the maximum difference in cavity and ambient pressure and the Helmholtz frequency  $\omega$  is defined in Eq. (13). If Eq. (23) is substituted into Eq. (22), an expression for maximum outflow velocity (or amplitude) can be obtained:

$$\bar{U}_{\max} = \Delta P / \rho_a \omega l \quad (24)$$

In the viscous regime, the flow is governed by the quasi-steady Poiseuille equation:

$$\bar{U} = \Pi R_o^2 / 8 \rho_a \nu \quad (25)$$

In this case, any oscillatory pressure behavior for the pressure-jump case will be suppressed by viscous effects and the maximum velocity is given by

$$\bar{U}_{\max} = R_o^2 \Delta P / 8 \rho_a \nu l \quad (26)$$

This result will also hold for the amplitude of the oscillating velocity for the synthetic jet.

Equations (24) and (26) can now be equated to provide an estimate for the optimal orifice radius:

$$R_{\text{opt}} = \left( \frac{64 \nu^2 l V}{\pi k T} \right)^{\frac{1}{6}} \quad (27)$$

Figure 7 shows a comparison between the predicted optimal orifice radii using Eq. (27) and numerical simulations. Good agreement is found at all scales  $g$ ; the analytical prediction underestimates by 14%. A correction factor  $c$  can be introduced into Eq. (27) to get exact agreement at all actuator scales, and it has been verified in Ref. 15 that this value ( $c = 1.14$ ) is design independent. In practice, Eq. (27) is more useful for the design of synthetic jets because for pressure-jump actuators it would usually be desirable to design out Helmholtz resonance, and this would determine the maximum orifice radius. [See Eq. (32) hereafter.]

An expression describing the behavior of optimized-velocity magnitude can be obtained by substituting Eq. (27) into the quasi-steady flow solution (26):

$$\bar{U}_{\text{opt}} \propto \Delta P (V/l^2)^{\frac{1}{3}} \quad (28)$$

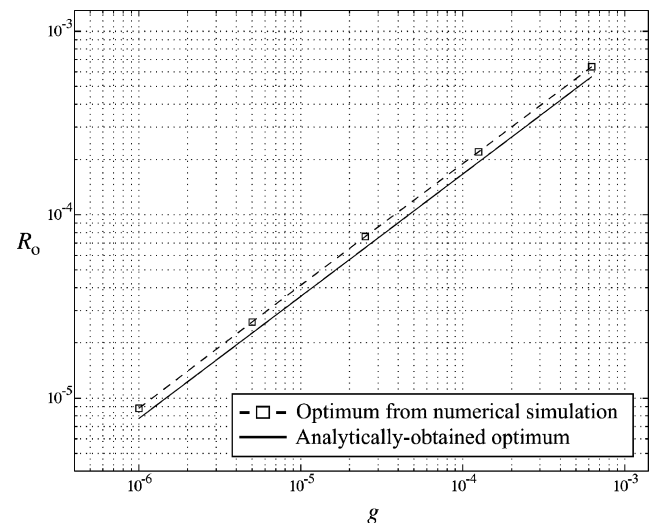


**Fig. 7** Variation of optimum  $R_o$  (optimized for maximum average velocity) with the characteristic length scale  $g$ ;  $\square$ , comparison of optimum from numerical simulations and  $---$ , analytically obtained optimum.

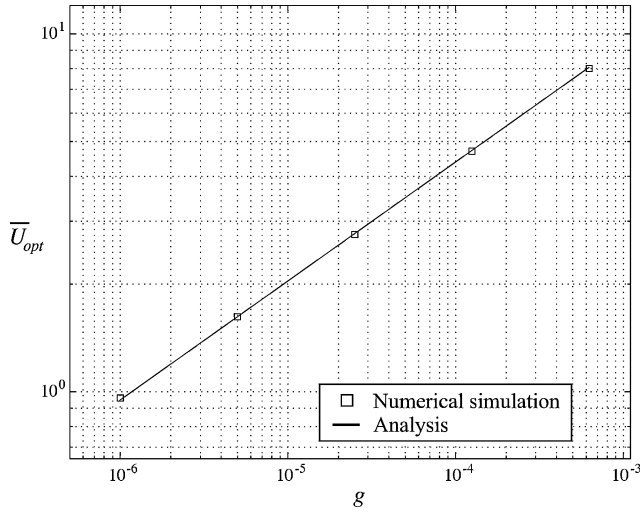


Fig. 8 Variation of optimized average velocity  $\bar{U}_{\text{opt}}$  with scale  $g$ ;  $\square$ , comparison of numerical simulation and —,  $\bar{U}_{\text{opt}} \propto g^{1/3}$ .

A quantitatively accurate analytical expression cannot be derived in this way. If the diaphragm is approximated as being instantaneously deflected, the pressure jump is given by

$$\Delta P = P_a \bar{w}_{\text{max}} / H \quad (29)$$

where  $\bar{w}_{\text{max}}$  is the maximum (over time) average (over space) deflection of the diaphragm. The combination of Eqs. (28) and (29) gives

$$\bar{U}_{\text{opt}} \propto \bar{w}_{\text{max}} (R_d / l H)^{2/3} \quad (30)$$

which can be reexpressed in terms of the characteristic length  $g$ :

$$\bar{U}_{\text{opt}} \propto g^{1/3} \quad (31)$$

This expression states that, provided all dimensions are scaled equally, the optimized velocity magnitude of a particular design is proportional to the cube root of its scale. This result is verified by the numerical model (Fig. 8).

#### Design Precepts

Expressions (28–30) can be used to describe general guidelines for design. From Eq. (28), it is clear that a linear relationship between the pressure jump and the maximum velocity exists. Together with Eq. (29), this implies that an optimal actuator should produce large diaphragm deflections within a shallow cavity. Furthermore, Eq. (30) suggests that the size of the diaphragm should be as large as possible.

The most successful synthetic-jet actuators have conformed to these simple design precepts. For example, the device used by Crook et al.,<sup>10</sup> which was optimized by a genetic algorithm, had a large diaphragm set within a shallow cavity ( $R_d / H \approx 6$ ).

Note that these expressions, though useful for describing general design principles, are based on a linear analysis and, therefore, are only valid for velocities of small magnitude.

#### Satisfying the Helmholtz Condition

In the preceding section, an expression was derived to evaluate the orifice radius at which Helmholtz oscillation would just occur, the Helmholtz condition:

$$R_o > c \left( \frac{12v^2 l V}{\pi k T} \right)^{1/6} \quad (32)$$

If the optimized orifice radius, given by Eq. (27), is substituted into the Helmholtz condition, it can be determined whether Helmholtz

oscillation will be present in velocity-optimized actuators:

$$c \left( \frac{64v^2 l V}{\pi k T} \right)^{1/6} > \left( \frac{12v^2 l V}{\pi k T} \right)^{1/6} \quad (33)$$

$$1.5 > 1$$

The condition is clearly satisfied, and, therefore, unforced oscillation will occur in velocity-optimized devices and, potentially, Helmholtz resonance also. Because this is undesirable, for reasons detailed earlier, it may be more appropriate to let the Helmholtz condition dictate the orifice size. These measures would dictate an orifice radius that would be one and one-half times smaller than that of a velocity-optimized actuator.

#### Conclusions

The design of MEMS actuators for turbulence control is at an early stage of development. There is, therefore, a requirement for numerically economical computational models. In this paper, such a model has been developed and successfully validated with experimental data. As far as we are aware, this represents the first time that an actuator of this type has been completely modeled from input voltage to output velocity. Although the model may not be quantitatively accurate for synthetic-jet devices (because there may be substantial cavity flow), it can accurately predict optimal device dimensions. It could, therefore, be used as an efficient design tool by synthetic-jet developers, and not just for MEMS-scale devices.

However, the model was developed for an alternative mode of diaphragm forcing, a constant as opposed to a sinusoidal load/voltage. Operation in this manner can create a disturbance that we believe is more suitable for the control of individual streaks and that does not suffer from the practical drawbacks of synthetic jets (the high risk of ingesting dust during the inflow cycle). This concept has been investigated in the current paper, where it has been demonstrated that given sufficient diaphragm damping, and the correct device dimensions, a pufflike output can be produced. In Ref. 15, it is shown that such a response can control individual streaks. These results will be detailed in future papers.

The pressure-jump actuator concept has been investigated from a design perspective. Simple expressions have been derived to determine the optimal device dimensions and to predict the optimized output. These have been verified with the numerical code. It is now possible to predict, in general terms, the effect of down-scaling this type of actuator. This information is useful, especially when designs intended for MEMS scale are prototyped at mesoscale or larger. The expressions have also identified some general design goals, such as the minimization of cavity height and the maximization of diaphragm radius.

There are other practical issues concerning the use of cavity-type devices for flow control. One of these is the potential for the cavity pressure to oscillate and, as a result, to be prone to Helmholtz resonance. This could produce unpredictable behavior in the actuator's environment, such as the promotion of unwanted disturbances in boundary layers.<sup>15</sup> In the present paper, it has been demonstrated that a device optimized for maximum velocity will not have sufficient orifice damping to cancel this phenomenon. This presents a serious design concern.


#### Acknowledgments

The research presented here was undertaken as part of the AEROMEMS project (an investigation into the viability of micro-electromechanical systems technology for boundary-layer control on aircraft), which is a collaboration between British Aerospace; Dassault Aviation; Centre National de la Recherche Scientifique; and the Universities of Warwick, Manchester, Berlin, Madrid, Athens, Lausanne, and Tel-Aviv. The project is managed by British Aerospace and is partially funded by the CEC under the IMT initiative (Project Ref. BRPR CT97-0573).

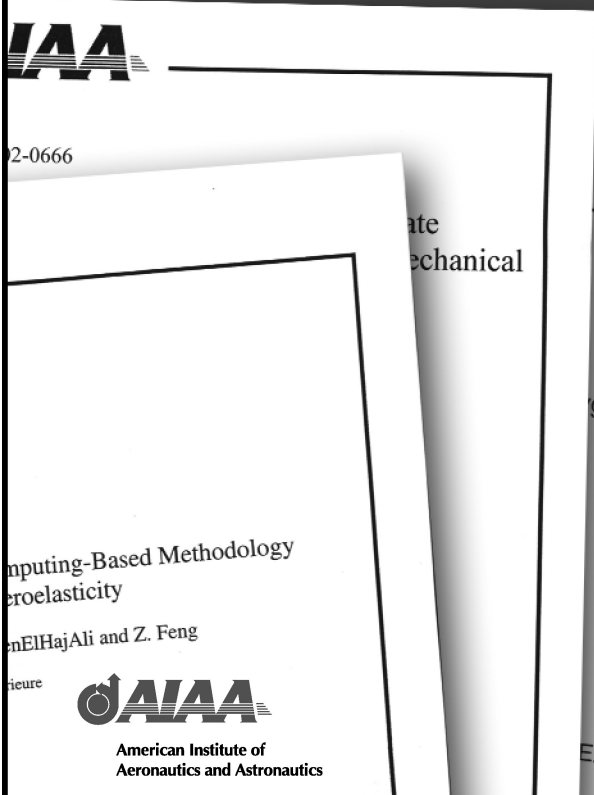
## References

- <sup>1</sup>Kline, S. J., Reynolds, W. C., Schraub, F. A., and Runstadler, P. W., "The Structure of Turbulent Boundary Layers," *Journal of Fluid Mechanics*, Vol. 30, 1967, pp. 741–773.
- <sup>2</sup>Blackwelder, R. F., and Eckelmann, H., "Streamwise Vortices Associated with the Bursting Phenomenon," *Journal of Fluid Mechanics*, Vol. 94, 1979, pp. 577–594.
- <sup>3</sup>Löfdahl, L., and Gad-el-Hak, M., "MEMS Applications in Turbulence and Flow Control," *Progress in Aerospace Sciences*, Vol. 35, 1999, pp. 101–203.
- <sup>4</sup>Rao, K., Narashima, R., and Badri Narayanan, M. A., "The Bursting Phenomenon in a Turbulent Boundary Layer," *Journal of Fluid Mechanics*, Vol. 48, 1971, pp. 339–352.
- <sup>5</sup>Blackwelder, R. F., and Haritonidis, J. H., "Scaling of the Bursting Frequency in Turbulent Boundary Layers," *Journal of Fluid Mechanics*, Vol. 132, 1983, pp. 87–103.
- <sup>6</sup>Johansson, A. V., Alfredsson, P. H., and Eckelmann, H., *Advances in Turbulence*, Springer-Verlag, Berlin, 1987.
- <sup>7</sup>Lighthill, M. J., "Acoustic Streaming," *Journal of Sound and Vibration*, Vol. 61, 1978, pp. 391–418.
- <sup>8</sup>Hassan, A. A., and JanakiRam, R. D., "Effects of Zero-Mass Synthetic Jets on the Aerodynamics of the NACA-0012 Airfoil," AIAA Paper 97-2326, 1997.
- <sup>9</sup>Smith, D. R., Amitay, M., Kibens, V., Parekh, D., and Glezer, A., "Modification of Lifting Body Aerodynamics Using Synthetic Jet Actuators," AIAA Paper, 98-0209, 1998.
- <sup>10</sup>Crook, A., Sadri, A. M., and Wood, N. J., "The Development and Implementation of Synthetic Jets for the Control of Separated Flow," AIAA Paper 99-3176, 1999.
- <sup>11</sup>Jacobson, S. A., and Reynolds, W. C., "Active Control of Streamwise Vortices and Streaks in Boundary Layers," *Journal of Fluid Mechanics*, Vol. 360, 1998, pp. 179–211.
- <sup>12</sup>Rathnasingham, R., and Breuer, K. S., "System Identification and Control of a Turbulent Boundary Layer," *Physics of Fluids*, Vol. 9, 1997, pp. 1867–1869.
- <sup>13</sup>Vandelli, N., Wroblewski, D., Velonis, M., and Bifano, T., "Development of a MEMS Microvalve Array for Fluid Control," *Journal of Micromechanical Systems*, Vol. 7, 1998, pp. 395–402.
- <sup>14</sup>Yang, F., and Kao, I., "Analysis of Fluid Flow and Deflection for Pressure-Balanced MEMS Diaphragm Valves," *Sensors and Actuators*, Vol. 79, 2000, pp. 13–21.
- <sup>15</sup>Lockerby, D. A., "Numerical Simulation of Boundary-Layer Control Using MEMS Actuation," Ph.D. Dissertation, School of Engineering, Univ. of Warwick, Coventry, England, U.K., March 2001.
- <sup>16</sup>Piekos, E. S., and Breuer, K. S., "Numerical Modelling of Micromechanical Devices Using the Direct Simulation Monte Carlo Method," *Journal of Fluids Engineering*, Vol. 118, 1996, pp. 464–469.
- <sup>17</sup>Gad-el-Hak, M., "The Fluid Dynamics of Microdevices — The Freeman Scholar Lecture," *Journal of Fluids Engineering*, Vol. 121, 1999, pp. 5–33.
- <sup>18</sup>Schaaf, S. A., and Chambré, P. L., *High Speed Aerodynamics and Jet Propulsion*, Vol. 3, Princetown Univ. Press, Princeton, NJ, 1958.
- <sup>19</sup>Ferziger, J. H., *Numerical Methods for Engineering Applications*, 2nd ed. Wiley-Interscience, New York, 1998.
- <sup>20</sup>Rizzetta, D. P., Visbal, M. R., and Stanek, M. J., "Numerical Investigation of Synthetic-Jet Flowfields," *AIAA Journal*, Vol. 8, 1999, pp. 919–927.
- <sup>21</sup>Rathnasingham, R., and Breuer, K. S., "Coupled Fluid-Structural Characteristics of Actuators for Flow Control," *AIAA Journal*, Vol. 35, 1997, pp. 832–837.
- <sup>22</sup>Dowling, A. P., and Ffowcs Williams, J. E., *Sound and Sources of Sound*, Ellis Horwood, Chichester, England, U.K., 1983.
- <sup>23</sup>Lockerby, D. A., Carpenter, P. W., and Davies, C., "Numerical Simulation of the Interaction of Microactuators and Boundary Layers," *AIAA Journal*, Vol. 36, No. 1, 2002, pp. 67–73.

W. J. Dahm  
Associate Editor


Register Purchase

# AIAA MEETING PAPERS ONLINE!




2-0666

ate  
mechanical

computing-Based Methodology  
eroelasticity

enElHajAli and Z. Feng

ieure



American Institute of  
Aeronautics and Astronautics

Each year, AIAA publishes more than 4000 technical papers presented at AIAA conferences. These papers contain the most recent discoveries in aerospace and related fields. No other organization offers this depth and breadth in the aerospace field.

**You now have immediate access to more than 20,000 technical papers online!**

Beginning with 1996 and adding about 4,000 papers every year, AIAA's online archive allows you to search for the latest developments in:

**Astrodynamics • Aerodynamics • Guidance • Structures • Fluids • Propulsion • Controls • Modeling and Simulation • Flight Mechanics • and more...**

Search and purchase only those papers that fit your needs. Papers are delivered in pdf format. Search by:

**Title • Keyword • Author • AIAA Paper Number • Conference Title • Publication Year**

Click on "Citations Database" from the AIAA Web site at

[www.aiaa.org](http://www.aiaa.org)